

Extending common envelope simulations from Roche lobe overflow to the nebular phase

Thomas A. Reichardt,^{1,2★} Orsola De Marco,^{1,2} Roberto Iaconi,^{1,2} Christopher A. Tout³ and Daniel J. Price⁴

¹*Department of Physics and Astronomy, Macquarie University, Sydney, NSW 2109, Australia*

²*Astronomy, Astrophysics and Astrophotonics Research Centre, Macquarie University, Sydney, NSW 2109, Australia*

³*Institute of Astronomy, University of Cambridge, Madingley Road, Cambridge CB3 0HA, UK*

⁴*Monash Centre for Astrophysics and School of Physics and Astronomy, Monash University, VIC 3800, Australia*

Accepted 2018 December 13. Received 2018 December 13; in original form 2018 September 5

ABSTRACT

We have simulated a common envelope interaction between a $0.88 M_{\odot}$, $90 R_{\odot}$, red giant branch star, and a $0.6 M_{\odot}$, compact companion with the smoothed particle hydrodynamics code, PHANTOM, from the beginning of the Roche lobe overflow phase to the beginning of the self-regulated inspiral, at three different resolutions. The duration of the Roche lobe overflow phase is resolution dependent and would lengthen with increased resolution beyond the ~ 20 yr observed, while the inspiral phase and the post-common envelope separation are largely independent of (average) resolution. Mass transfer rates through the Lagrangian points drive the orbital evolution during the Roche lobe overflow phase, as predicted analytically. The absolute mass transfer rate is resolution dependent, but always within a factor of two of the analytical value. Similarly, the gravitational drag in the simulations is close to the analytical approximation. This verifies simulations and shows that these analytical approximations are reasonable. The L_2 and L_3 outflows observed during Roche lobe overflow remain bound, forming a circumbinary disc that is largely disrupted by the common envelope ejection. However, a longer phase of Roche lobe overflow and weaker common envelope ejection typical of a more stable Roche lobe phase may result in a surviving circumbinary disc. Finally, we examine the density distribution resulting from the interaction for simulations that include or omit the phase of Roche lobe overflow. We conclude that the degree of stability of the Roche lobe phase modulates the shape of the subsequent planetary nebula, explaining the wide range of post-common envelope planetary nebula shapes observed.

Key words: hydrodynamics – stars: AGB and post-AGB – binaries: close – stars: evolution – planetary nebulae: general.

1 INTRODUCTION

The common envelope interaction is a phase of binary stellar evolution invoked to describe a dramatic decrease in the orbital separation of two stars, coupled with the ejection of a large amount of gas. The idea is attributed to Paczynski (1976, by whom private communications with Ostriker and Webbink are also credited), who was attempting to explain the origin of some compact, evolved binaries. As the primary, more massive star in an intermediate separation binary system swells to become a red giant, it transfers mass to its companion in a phase of Roche lobe overflow. If the mass transfer is unstable, the companion is likely swallowed by

the expanding outer atmosphere of the primary. What follows is a phase of dramatic reduction in the orbital separation on a dynamical time-scale, after which the envelope is presumably ejected to reveal a compact binary composed of the companion and the core of the giant primary. If the envelope is not ejected then it is expected that the stars will eventually merge.

Understanding this interaction is critical to the interpretation of binary phenomena, from intermediate luminosity red transients (e.g. Blagorodnova et al. 2017) to determining the nature of the progenitor of type Ia supernovae (e.g. Toonen & Nelemans 2013), and to illuminating the evolutionary path that leads to compact neutron star and black hole systems that can eventually merge by emission of gravitational waves (e.g. Abbott et al. 2016). See De Marco & Izzard (2017) for a review.

* E-mail: thomas.reichardt@students.mq.edu.au

Several observed objects carry characteristics distinctive of the common envelope interaction and have been interpreted as common envelope mergers. While some have been known for a while (V838 Monocerotis, Bond et al. 2003), many more are being discovered now, with the intensification of time-resolved observations. V1309 Sco (Tylenda et al. 2011) was interpreted as the merging of a solar-mass subgiant with a much less massive companion. M31-2015LRN (MacLeod et al. 2017a), and possibly V838 Mon, were likely slightly more massive, in the range of 3–5.5 M_{\odot} . M101-OT (Blagorodnova et al. 2017) possibly came from an 18 M_{\odot} progenitor, while NGC 4490-OT (Smith et al. 2016) might have derived from an even more massive star. This flurry of observations promises to place much needed constraints on common envelope simulations, which in turn can start to give physical explanations to these phenomena (Galaviz et al. 2017).

Simulations of the common envelope interaction utilizing a variety of codes have, with some success, reproduced observable post-common envelope system parameters. A non-exhaustive list of recent works includes adaptive mesh refinement (AMR) simulations (Ricker & Taam 2012), comparisons of smoothed particle hydrodynamics (SPH) and grid techniques (Passy et al. 2012; Iaconi et al. 2017), SPH simulations examining the inclusion of recombination energy (Nandez, Ivanova & Lombardi 2015) and moving-mesh simulations (Ohlmann et al. 2016). Most simulations model lower mass red giant branch (RGB) stars and thereby only cover a limited section of the parameter space. In addition, simulations typically start with the companion very close to the surface of the star and stop as soon as the orbital distance has stabilized. This leaves open the question of whether the phases preceding the dynamic inspiral have an effect on the inspiral itself, on the parameters of the post-common envelope binaries, including the ejecta or nebula that may derive from it, and on the light properties near the time of the outburst.

The effect of starting common envelope simulations at primary Roche lobe contact was investigated by Iaconi et al. (2017), who concluded that including the unstable Roche lobe overflow phase leads to a marginally wider final separation. They also showed that starting the simulations at a wider separation does not increase the amount of unbound common envelope mass.¹ However, they did not investigate the outflow, nor the details of the early, pre-dynamical, and inspiral. In one of their simulations, carried out with the SPH code PHANTOM (Price et al. 2018), they noticed that the relatively long phase of Roche lobe overflow, before the fast inspiral, resulted in the ejection of some mass from the second and third Lagrangian points, L_2 and L_3 . This raised the suspicion that the modelled common envelope ejecta would differ from when the simulation starts at smaller orbital separations, something that could impact studies of the nebular shapes resulting from common envelope ejections (Frank et al. 2018; García-Segura, Ricker & Taam 2018).

Observations already indicate that phases just before the dynamical common envelope may play a role in the overall outcome of the interaction. For example, V1309 Scorpii was captured in the OGLE-III and OGLE-IV (Optical Gravitational Lensing Experiment) fields

between 2001 and 2008, when the system displayed reduction in the orbital period, before undergoing a fast brightening of several magnitudes (Tylenda et al. 2011). Before the outburst, the object steadily brightened over 3 yr. These time-scales and the concomitant characteristics of the contact binary periodic variability are not easily explained with a common envelope dynamical phase, implying a slower interaction leading up to fast dynamical common envelope merger.

In order to explain the slower, pre-outburst rise of V1309 Sco, Pejcha, Metzger & Tomida (2016), Pejcha et al. (2017), and Metzger & Pejcha (2017) took a different approach to simulating common envelope transients. Their study targeted the light curve of a contact binary before inspiral. By simulating the flow through the L_2 point, they claimed to have identified the cause of the slow pre-outburst light increase in V1309 Sco, as well as of other characteristics of transient light curves. They did not comment on the effects of L_2 mass loss on the subsequent phase of dynamical inspiral, but the implication is that the two phases are intimately connected.

MacLeod, Ostriker & Stone (2018a,b) presented additional simulations of the Roche lobe overflow phase leading up to a common envelope inspiral. They simulated a binary system with a mass ratio of $M_2/M_1 = 0.3$, initialized at the analytic Roche limit separation of $2.06R_1$, where R_1 is the radius of the primary star. The simulation was not continued past the beginning of the dynamic inspiral. They showed the decay of the orbit to be driven by exchange of angular momentum from the companion to the mass flow, which is then lost from the system through the L_2 point. MacLeod et al. (2018a) claimed that, contrary to what was concluded by Pejcha et al. (2017), mass lost through the L_2 point is not unbound until much later in the simulations, when the companion is almost in contact with the primary. This bound outflow forms a large disc of material in the orbital plane, which collimates the late time unbinding, forming a bipolar gas distribution.

Much is yet to be learned about the common envelope interaction itself and the transient phenomena that it causes. Including an extended phase of mass transfer and following the distribution of ejecta after the dynamic inspiral moves us towards an integrated understanding of these adjacent phases.

In Section 2, we summarize the set-up for our simulations. In Section 3, we give an overview of the simulation behaviour and discuss the effect of increasing resolution on our simulations, along with the conservation of energy and angular momentum. In Section 4, we investigate the pre-inspiral phase of our simulations, comparing numerical mass transfer rates during Roche lobe overflow with the behaviour predicted analytically. Further, we discuss the different processes contributing to the reduction in orbital separation both before and during the dynamic inspiral. We also discuss the creation of acretion disc, and the presence of fallback material. Section 5 contains a discussion of the formation of planetary nebulae (PNe) from common envelopes, and the applications of our final gas distributions to further simulations. We conclude and summarize in Section 6.

2 INITIAL CONDITIONS

The simulations presented here follow on from work done by Passy et al. (2012) and Iaconi et al. (2017). The simulations we analyse include one that was already presented by Iaconi et al. (2017), who list further details. In summary, we modelled a binary system made of a 0.88 M_{\odot} , 90 R_{\odot} RGB primary with a 0.392 M_{\odot} point mass core in orbit with a 0.6 M_{\odot} point mass companion. We used three

¹Envelope unbinding remains an issue, although some solutions or partial solutions have started appearing in the literature. Recent discussions have turned towards the ability of recombination energy to act as a source of energy (Han, Podsiadlowski & Eggleton 1994), allowing further envelope unbinding (see e.g. Ivanova 2018 and the counter arguments of Grichener, Sabach & Soker 2018; Soker, Grichener & Sabach 2018).

Table 1. Comparison of SPH particle smoothing lengths, denoted here as h , for each of our different resolution simulations. The subscripts min and max refer to the outer limits of the range of h , while subscript 90 denotes the h below which 90 per cent of particles lie. Subscript 0 refers to the beginning of the simulation, while subscript *ins* refers to the time of fastest descent during the dynamic inspiral (6.4, 8.7, 13.3, and 18.0 yr for the low-, medium-, and high-resolution and corotating simulations, respectively).

n_{part}	$h_{\text{min}; 0}$ (R_{\odot})	$h_{\text{max}; 0}$ (R_{\odot})	$h_{\text{min}; \text{ins}}$ (R_{\odot})	$h_{90; \text{ins}}$ (R_{\odot})	$h_{\text{max}; \text{ins}}$ (R_{\odot})
8.0×10^4	0.52	14	0.43	170	1.0×10^4
2.3×10^5	0.35	11	0.35	75	1.2×10^4
1.1×10^6	0.19	8.7	0.19	34	1.9×10^4
2.3×10^5 †	0.35	11	0.26	390	2.0×10^4

Note: † Simulation with corotating primary.

different resolutions of 8×10^4 , 2.3×10^5 , and 1.1×10^6 SPH particles. In addition to these simulations, a 2.3×10^5 particle simulation was also evolved with a primary star in corotation with the orbit. The resolution length in SPH, the smoothing length, is related to the local number density of particles. Initially, SPH particles in our high-resolution simulation have smoothing lengths ranging between 0.2 and $9 R_{\odot}$. For more details on the smoothing lengths in the different simulations, refer to Table 1.

The core of our giant star and the companion are represented by point masses. These particles do not have associated internal energies or pressures, instead interacting purely gravitationally with other particles in the simulation. Their gravitational potentials have been softened by a cubic spline kernel, with a softening length of $3 R_{\odot}$. This means that within a radius of $3 R_{\odot}$, the potential of the point mass particles is almost flat (for more information on the exact process, see Price et al. 2018), and outside a radius of twice the softening length, the potential is exactly the analytical form. Softened potentials are typically used when point mass particles are not allowed to accrete gas, which is the case in our simulations.

Before the binary simulations are carried out, the primary star is relaxed in the computational domain, as explained by Iaconi et al. (2017). This tends to result in a stellar structure with a slightly larger radius. The relaxed radii differ marginally with resolution, being 87, 91, and $93 R_{\odot}$ for the low, medium, and high resolutions, respectively. We also note that we use the volume-equivalent radius (defined by Nandez, Ivanova & Lombardi 2014 to be the radius of a sphere with the total volume occupied by particles) for gas with a higher density than the initial lowest density in the star.

The corotating simulation starts with a non-rotating primary star stabilized in the inertial frame. The star is then placed with its companion in the corotating frame. As a result, the primary is effectively instantaneously spun up. The primary is somewhat distorted by the sudden introduction of the companion and it expands due to the rotation. This may lead to a larger mass transfer rate, which we will address in Section 4.1.2. We were unable to perform all the simulations in the corotating frame, because the length of the Roche lobe overflow phase is approximately doubled, causing the simulations to take a prohibitively long time to complete.

We chose the initial orbital separation such that the Roche lobe of the giant is approximately equal to its stellar radius. With our parameters, the initial orbital separation is about $218 R_{\odot}$ [by equation (2) of Eggleton 1983]. With this setup, a phase of mass transfer begins immediately upon starting the simulation.

There are at least two effects that contribute to a binary entering a phase of Roche lobe overflow: a star expands as it evolves into a giant, eventually filling its Roche lobe; or the system’s orbital

separation may also decrease, such that the Roche lobes shrink and can eventually match the stellar radius. The reduction in separation for systems that are started well outside of Roche lobe contact is, in nature, driven by tidal interactions from distortions of the primary envelope by the potential of the secondary. This is also true in simulations, although the orbital decay tends to be unrealistically rapid, possibly because the tidal dissipation couples with the numerical viscosity scale, or because of oscillations artificially set in motion by the initial conditions. This said, starting the simulation with an orbital separation larger than $218 R_{\odot}$ results in a far more stable orbit and it requires longer simulation times to initiate mass transfer.

The simulations of MacLeod et al. (2018b,a) used similar initial conditions as our own and aim to address similar questions. We will therefore make some specific comparisons between the two sets throughout this paper.

3 SIMULATION OVERVIEW

We first present an overview of the simulation parameters and their dependence on resolution, as well as conservation properties. We use this as a basis to describe the orbital evolution in Section 4. We show a visual overview of the simulation behaviour in Fig. 1. In the top three panels, the system is undergoing Roche lobe overflow. The bottom three panels show the evolution of the system within a year from beginning the dynamic inspiral.

3.1 System evolution

The two left-hand columns of Fig. 2 shows the density evolution in the orbital plane (left) and along the plane perpendicular to the orbital plane (right) as a snapshots in time (top to bottom) for the 1.1 million particle simulation. The two right-hand columns of Fig. 2 shows the corresponding velocity slices.² At the start of the simulation, gas moves in a stream from the primary to the companion. This stream does not flow exactly through the inner Lagrange point L_1 , instead flowing slightly around it. This can be explained by the star not being in corotation with the orbit, which is further evidenced by the fact that the stream does flow through the L_1 point in the corotating simulation. Some of this mass collects in a small disc around the companion, while the orbital separation decreases and the mass transfer rate increases. Gas starts flowing out of the system via the outer Lagrange point L_2 and eventually through L_3 . These outflows are visible in Fig. 2 as spiral tails extending from both point masses in the orbital plane. The L_2 outflow is present to the right of the companion (right-hand green dot) in the top four rows. The L_3 outflow is most prominent in the second and third rows of Fig. 2 as a tail extending from the left of the primary.

Later, the companion is engulfed in the atmosphere of the donor star and the common envelope inspiral starts, eventually finishing on a dynamical time-scale and leading to a rapid reduction in the orbital separation (bottom row of Fig. 1 and last two rows in Fig. 2). As the companion is engulfed, a shell of material is ejected above escape velocity, becoming unbound. More material is unbound as the inspiral continues, but most of the envelope is only lifted to larger radii, remaining bound. This is consistent with the findings of Iaconi et al. (2018), that most of the unbound ejecta is from the surface of the donor star and is lost at the beginning of the

²In later figures, we will zoom-in on various parts of the simulations to clarify different aspects of the flow.

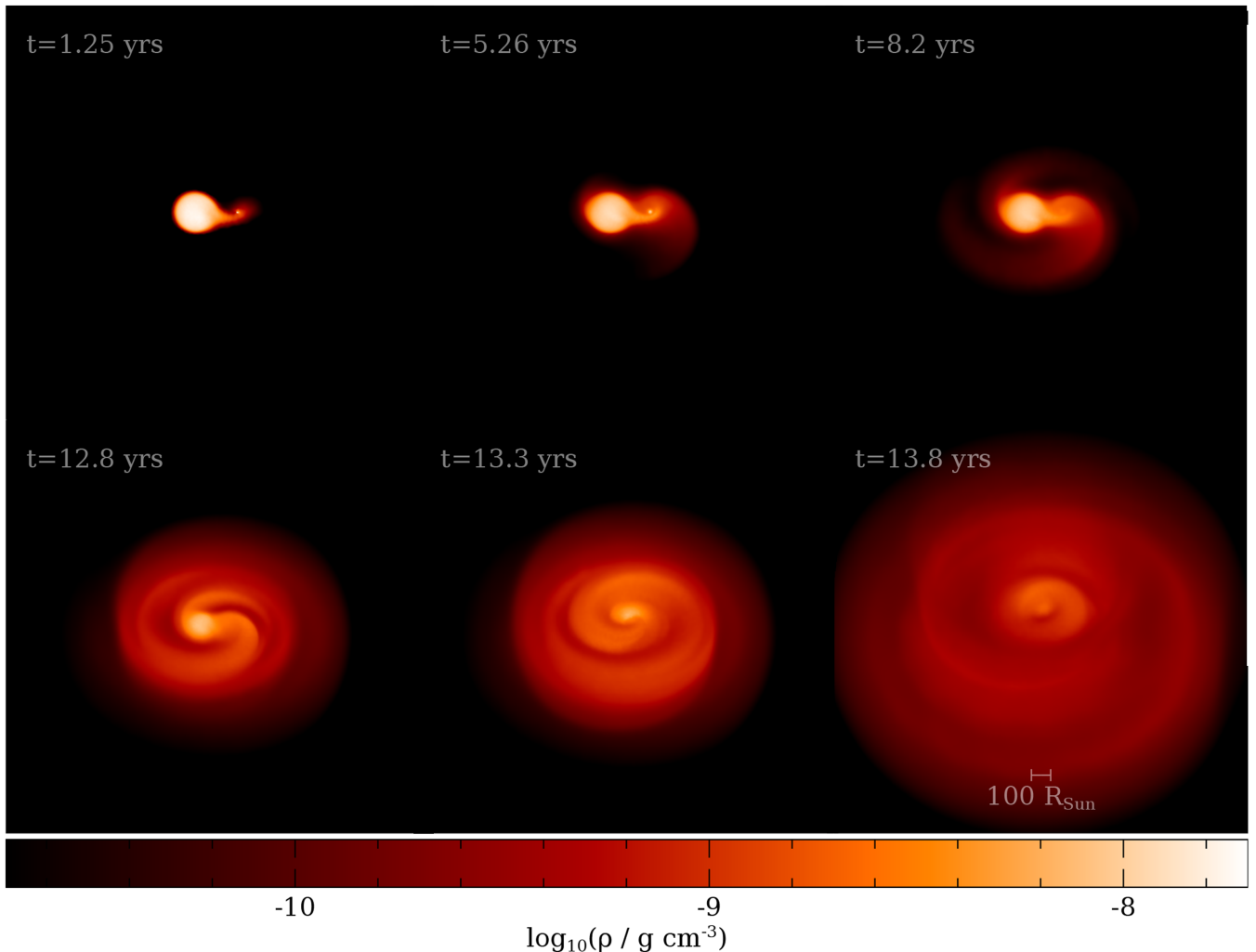


Figure 1. Surface rendering of our 1.1 million particle simulation. The frames are au per side. From left to right and top to bottom, each panel is a snapshot taken at 1.25, 5.26, 8.2, 12.8, 13.3, and 13.8 yr. This is intended to display the overall evolution of the simulation. This image, along with all other renderings of the simulation in this paper, was created with SPLASH (Price 2007). In surface renderings such as this, a value for the opacity is assigned arbitrarily for the desired visual result. In this case, $\kappa = 1.9 \times 10^{-9} \text{ cm}^2 \text{ g}^{-1}$.

dynamic inspiral. The mass that is ejected collides with material that previously flowed out through the L_2 and L_3 points, shaping the common envelope (we discuss this further in Section 5.1).

Due to evacuation of gas within the orbit of the far more compact binary, and a reduced velocity contrast between the cores and the gas due to the envelope being dragged into corotation, the inspiral slows down dramatically. There is still some interaction, hence the cores do not fully halt in their radial migration. Further, during this extended phase of slow inspiral, we begin to witness a partial fallback of some of the gas that was not fully unbound (see Section 4.4).

3.2 Resolution study

To see whether our results are sensitive to numerical resolution, we performed a resolution study. Because the highest resolution simulation, at 1.1 million SPH particles, required approximately 10 months on a hyper-threaded 16 core server (approximating a 32 core server), increasing the resolution further is currently unfeasible. Instead, we compared our simulation with a series of lower resolution calculations. Table 1 lists the particle numbers and

the corresponding minimum- and maximum-resolution lengths (the SPH smoothing length) in each simulation, both at the beginning of the simulation (second and third columns) and during the dynamical inspiral (fourth, fifth, and sixth columns). It should be noted that the smoothing length of a particle scales inversely and smoothly with density. Hence, the simulations are most well resolved around the cores, where the gas is most dense. We observe that the 1.1 million particle simulation has smoothing lengths typically smaller than half that of the 80 000 particle simulation, except for the outer portions of the initial star.

A comparison of the three simulations shows that the orbital separation at the end of the fast inspiral and the average rate of descent during the fast inspiral appear converged with respect to numerical resolution (see Table 2). These values were determined from the simulations by defining the dynamic inspiral to be when $|\frac{\dot{a}}{a}| \geq \frac{1}{15} \max |\frac{\dot{a}}{a}|$ holds true. For more discussion of the time-scales, see Section 4.1.1. The full orbital evolution of the simulations is shown in the top panel of Fig. 3. The length of the mass transfer phase, marked by the vertical grey lines in Fig. 3, increases with resolution and stellar rotation.

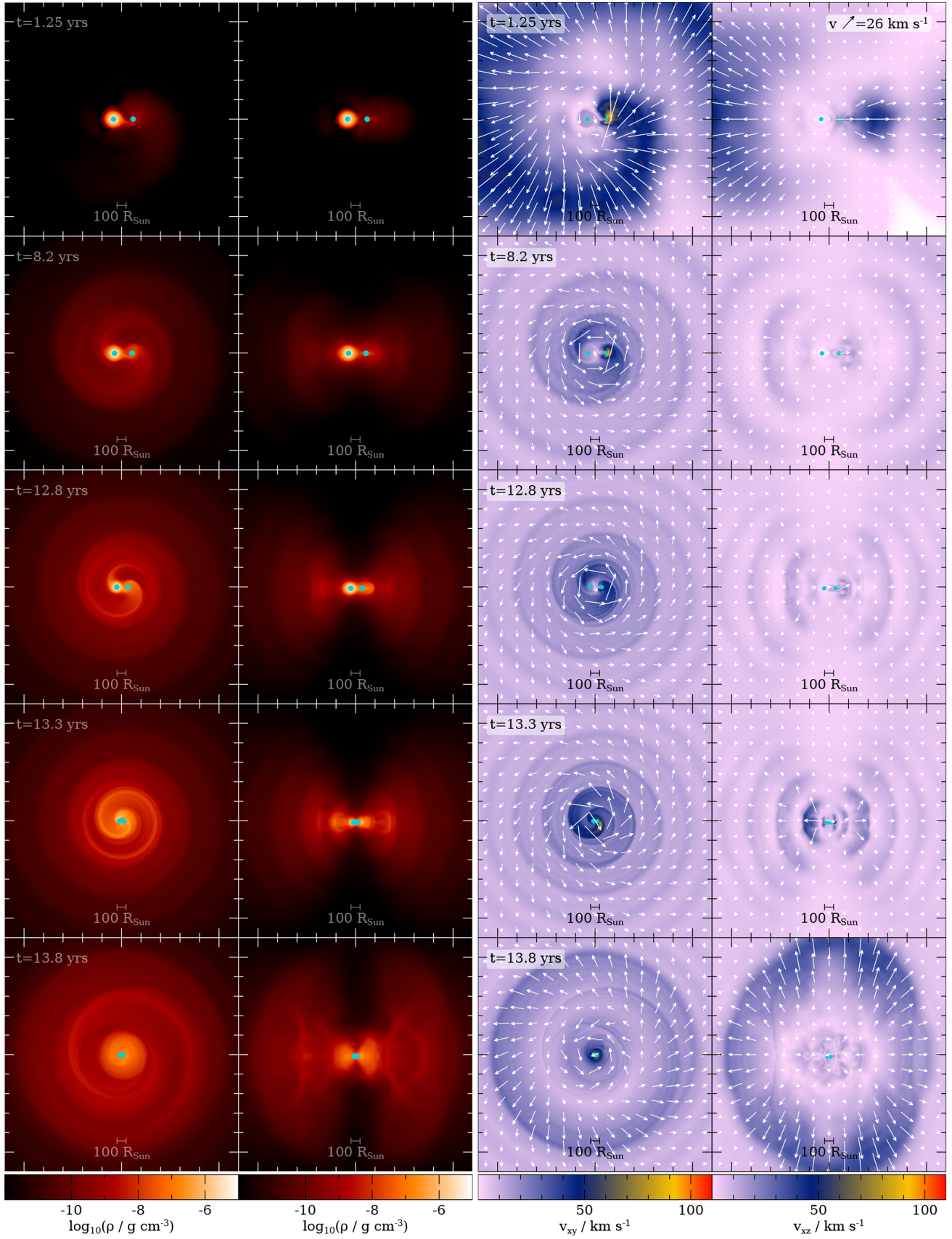


Figure 2. Columns 1 and 3: density and velocity slices in the orbital plane, respectively. Columns 2 and 4: density and velocity slices in the perpendicular plane, respectively. Arrows show the direction and relative magnitude of the velocity. Each frame is 12 au on each side and was taken from our 1.1 million particle simulation. The two point mass particles are plotted as green points, with the primary to the left and companion to the right. From top to bottom, each row is a snapshot taken at 1.25, 8.2, 12.8, 13.3, and 13.8 yr.

Table 2. Comparison of orbital evolution quantities for different resolutions. Here, we choose a as the orbital separation, m_u as the unbound mass, $m_{\text{tot}} = 0.49 M_\odot$ as the total gas mass in the simulation, and t as the time. The subscripts i and f refer to times at the beginning and end of the fast inspiral as defined in the text, respectively. The subscript p refers to the ‘plateau’ value of the unbound mass, after the end of the fast inspiral. $\frac{\Delta a}{\Delta t}$ is the mean rate of descent during the fast inspiral.

n_{part}	a_i (R_\odot)	a_f (R_\odot)	$t_f - t_i$ (d)	$\frac{\Delta a}{\Delta t}$ ($R_\odot \text{ d}^{-1}$)	$m_{u, i}$ (M_\odot)	$m_{u, p}$ (M_\odot)	$\frac{m_{u, p}}{m_{\text{tot}}}$ $\times 100$	$m_{u, i}^*$ (M_\odot)	$m_{u, p}^*$ (M_\odot)	$\frac{m_{u, p}^*}{m_{\text{tot}}}$ $\times 100$
7.6×10^4	130	30	276	0.36	0.045	0.157	32.2	0.053	0.160	32.9
2.3×10^5	126	28	275	0.36	0.011	0.071	14.6	0.013	0.076	15.6
1.1×10^6	122	28	263	0.36	0.001	0.050	10.3	0.002	0.054	11.1
$2.3 \times 10^5 \dagger$	129	31	354	0.28	0.046	0.092	18.9	0.048	0.097	19.9

Notes: \dagger Simulation run with corotating primary.

* Unbound criterion includes internal energy.

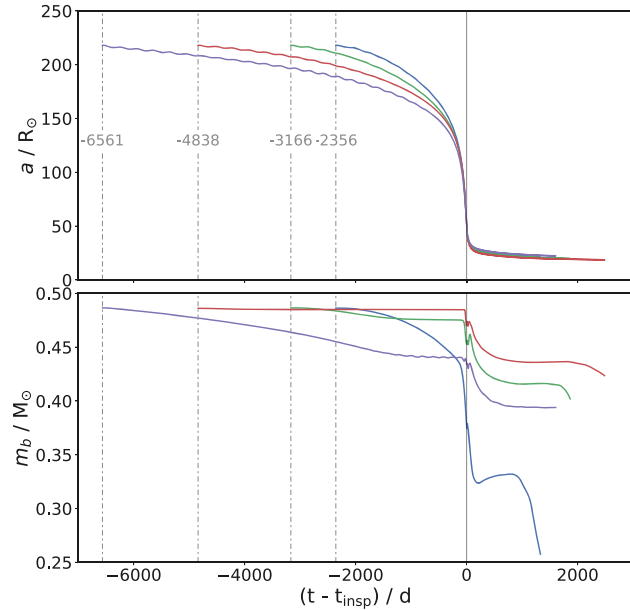


Figure 3. Comparison of the orbital evolution (top panel) and bound mass (bottom panel) for simulations with differing resolutions. Resolutions are 8×10^4 particles (blue), 2.3×10^5 particles (green), and 1.1×10^6 particles (red). The 2.3×10^5 particle simulation was also run with a corotating primary (purple). The simulations have been shifted such that they line up at $t = t_{\text{insp}}$, which is the time when \dot{a}/a , where a is the orbital separation, is at a minimum (see Section 4.1.1).

Table 2 also gives the amount of unbound material in our simulations, which is resolution dependent. In this work, we use the sum of kinetic and potential energies to determine unbound particles (if $E_{\text{kin}} + E_{\text{pot}} > 0$, the gas is unbound from the system). This gives a lower limit to the unbound mass. In some works, the internal (thermal) energy is also considered ($E_{\text{kin}} + E_{\text{pot}} + E_{\text{int}} > 0$), which leads to a somewhat greater amount of unbound gas. We include the amounts of unbound mass calculated with both criteria in Table 2, but we infer that even including internal energy in the unbound criterion, the amount of unbound mass does not increase significantly. This is also supported by the results of Staff et al. (2016a).

Fig. 3 (bottom panel) compares the mass of bound material for our three resolutions. Higher resolution simulations unbind less material. Gas is primarily unbound during the fast inspiral, although a small amount is unbound before, during Roche lobe overflow. This pre-inspiral unbinding is smaller at higher resolution, with the high-resolution simulation unbinding only

$0.05 M_\odot$ before the inspiral. Comparing the inertial and corotating frame simulations at intermediate resolution, we see that the pre-inspiral unbinding is greater for rotating stars. The length of the pre-inspiral phase does not appear to have converged at the resolutions we have tested, meaning that it could be longer in reality.

Further, each of the simulations begins to experience renewed unbinding shortly after the time of orbital stabilization. For the high-resolution simulation, this begins to take place shortly before we stop the simulation (hence is not seen in Fig. 3), much longer after stabilization than for the lower resolution simulation. This unbinding event is somewhat deceptive, in that it does not represent a large shift in the energy of particles that become unbound. In other words, particles that are close to the threshold of being unbound receive relatively small boosts in kinetic energy, from the orbital energy of the two cores, pushing the particles just over the threshold. Although the exact cause is unclear, this resolution-dependent unbinding occurs approximately when the softening radius of the point masses is no longer resolved in the simulation, which happens when the local smoothing length of the gas particles exceeds the softening radius. This occurs at late times because of the decreasing gas density surrounding the remnant cores.

3.3 Energy and angular momentum conservation

Our simulations employed a single, global time-step for all particles, which leads to excellent conservation of energy and angular momentum, at the cost of computational speed. Both physical quantities are conserved to better than 0.1 per cent, an improvement on prior SPH simulations (e.g. the 1 per cent conservation observed in the common envelope simulations of Passy et al. 2012). Figs 4 and 5 show the components of energy and angular momentum in our highest resolution simulation. Conservation is approximately 0.1 per cent and 0.3 per cent for our medium- and low-resolution simulations, respectively.

In Figs 4 and 5, we plot multiple quantities as a direct comparison to the equivalent figures in Passy et al. (2012). For much of the simulation, none of the components vary significantly. Our primary core and companion particles do not possess internal energy because they interact with the SPH particles only gravitationally. Hence, the total internal energy is summed over only the gas particles. All other quantities are found by summing components from gas and point mass particles as needed. Of note is that the envelope energy, calculated as the sum of the envelope potential energy, the total internal energy, and the bound kinetic energy, begins negative and remains so for the entire simulation. The fact that by the end of the simulation the average total energy of the envelope is close to zero

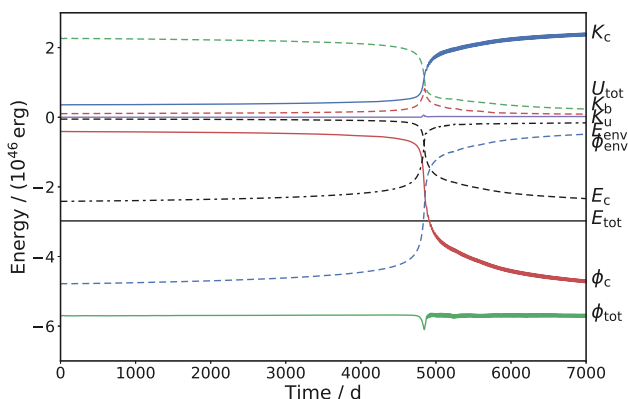


Figure 4. Evolution of the energy components. Here, K_c (solid blue) is the total kinetic energy of the two cores, U_{tot} (dashed green) is the total internal energy of the gas, K_b (dashed red) is the kinetic energy of bound gas, K_u (purple) is the unbound kinetic energy, E_{env} (dotted–dashed black) is the envelope energy, ϕ_{env} (dashed blue) is the potential energy of the envelope, E_c (dashed black) is the orbital energy of the cores, E_{tot} (solid black) is the total energy of the system, ϕ_c (solid red) is the potential energy between the point mass particles, and ϕ_{tot} (solid green) is the total potential energy.

suggests that the envelope is only marginally bound. It is possible that with the help of part of the recombination energy budget this may lead to complete unbinding of the envelope.

Fig. 5 shows only the z -components of the angular momentum (with respect to the centre of mass of the system at the beginning of the simulation, located at the origin, because the majority of rotational motion is in the orbital plane of the system). We plot the angular momentum of the bound and unbound gas, as well as the angular momentum of the two cores. There is a slight peak in the angular momentum curve of the bound mass. This is because, after this point, some mass becomes unbound. The excellent conservation gives an indication that the transfer of angular momentum is being handled correctly within our simulation. The analytical equation for the angular momentum of a binary system is

$$J = M_1 M_2 \left(\frac{Ga}{M} \right)^{\frac{1}{2}}, \quad (1)$$

where M_1 , M_2 , M , a , and G are the primary and secondary star masses, the total mass of the system, the orbital separation, and the gravitational constant, respectively. Using this, we calculate a total angular momentum budget of 3.87×10^{52} erg s. This is consistent with that calculated directly from the simulation.

3.4 The corotating reference frame

One of our two simulations with an intermediate resolution (2.3×10^5 particles) was carried out in a frame of reference rotating with the initial angular velocity of the system. However, the primary star was stabilized in isolation in the *inertial* reference frame. Only then were the primary and companion placed in the corotating frame. All gas SPH particles were set to be initially stationary in this frame. We did not stabilize the primary giant alongside its companion in the corotating frame, something that will be included in future simulations.

In the corotating frame, the tidally locked star overfills its Roche lobe more than for the corresponding inertial frame simulation, leading to an initially larger mass transfer rate. On the other hand, this simulation progressed more slowly, with a time-scale approxi-

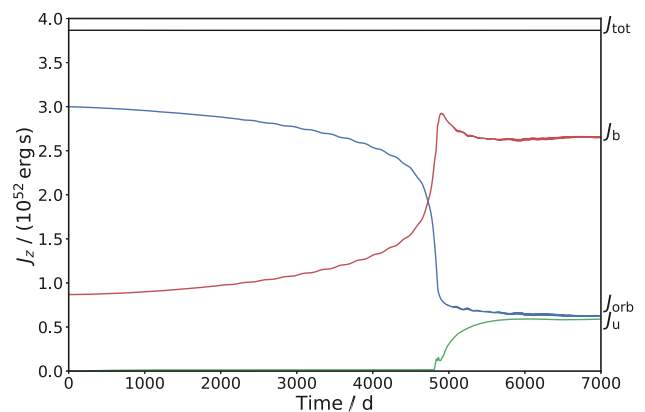


Figure 5. Evolution of the angular momentum components. In this plot: J_b (red line) is the angular momentum of bound gas, J_{orb} (blue line) is the angular momentum of the point mass particles, J_u (green line) is the angular momentum of unbound material, and J_{tot} (black line) is the total angular momentum in the simulation.

mately double that of the equivalent inertial frame simulation. This is because giant star gas begins the simulation with greater angular momentum, hence the envelope gas requires less additional angular momentum to be ejected. As a result, the companion exchanges a smaller amount of orbital angular momentum to the envelope before the gas is ejected. This results in a slower decrease in orbital separation.

As a binary system enters the dynamical inspiral, the relative velocity between the companion and the gas increases, but due to the initial rotation of the primary, the gas is dragged into corotation with the cores more rapidly than for the inertial frame simulation. Hence, the orbit enters the self-regulated inspiral at $31 R_{\odot}$, a slightly larger separation than $28 R_{\odot}$, measured from the equivalent, non-rotating simulation. The mean rate of inspiral is also slower in the corotating simulation (compare 0.28 and $0.36 R_{\odot} \text{ d}^{-1}$ in Table 2). Energy and angular momentum in the rotating reference frame simulation are conserved at the level of 1 and 0.1 per cent, respectively.

4 ORBITAL EVOLUTION

Having discussed the numerical aspects of the simulation, we here describe in detail the phases of our simulation that were outlined in Section 3.1.

4.1 Roche lobe overflow

We start by analysing the behaviour of the binary during the Roche lobe overflow phase that leads to the dynamical inspiral. We are interested in the rate of decrease of the orbital separation, the mass transfer rate as a function of time, the formation of circumbinary structures, and the overall length of the pre-inspiral interaction.

4.1.1 Orbital evolution time-scale

The giant primary is not in perfect equilibrium at the start of the simulation because it is not stabilized in the potential of the companion. The resulting distortions to the primary envelope are small, but none the less lead to an orbital evolution that is too fast. In addition, the rate at which the Roche lobe overflow phase proceeds and how quickly the system enters a common envelope, depends on resolution (see Fig. 3). At our lowest resolution of approximately

80 000 SPH particles, the Roche lobe overflow phase progresses in about half the time required for our high-resolution simulation of 1.1 million particles. This demonstrates that the length of the Roche lobe overflow phase has not converged. This reaction to the new potential is also likely to be the cause of the initial mild eccentricity that develops early in the simulation, visible in Fig. 3.

Mass transfer between the stars and mass loss from the L_2 and L_3 locations drives orbital shrinkage (see equation 2), and it is likely affected by resolution, because the mass is discretized differently. Below we compare the inverse of the orbital time-scale, \dot{a}/a , calculated purely from the orbital separation of the two cores in the simulation, with the value derived from equation (1) and Kepler's third law:

$$\frac{\dot{a}}{a} = \frac{2\dot{J}}{J} - \frac{2\dot{M}_1}{M_1} - \frac{2\dot{M}_2}{M_2} + \frac{\dot{M}_1 + \dot{M}_2}{M_1 + M_2}, \quad (2)$$

where the symbols have the same meaning as in equation (1).

In equation (2), we use the mass contained in the primary and companion Roche lobes (M_1 and M_2 , respectively). For the angular momentum J , we sum the contributions from the two core particles and the angular momentum of the gas inside the Roche lobes of the binary, all with respect to the centre of mass. During the interaction, gas is expelled from the Roche lobes of the binary, forming the spiral density arms visible in Fig. 2. The angular momentum carried off in the spiral waves drives the decrease in orbital separation. It should be noted that the separation should decrease even if $\dot{J} = 0$, as long as $M_1 > M_2$ and $\dot{M}_2 = -\dot{M}_1$. The disc formed by this outflow is discussed in Section 4.1.3.

We measure \dot{M}_1 and \dot{M}_2 by calculating the change in the number of SPH particles inside the Roche lobes of the primary and companion, respectively. The Roche lobe radius is updated at every code output to reflect the changes in orbital separation and stellar masses. This method of measuring the change in stellar mass is an approximation because, for example, it does not take into account particles that enter the companion's Roche lobe, but exit it before the next code output.

The simulated and analytically derived time-scales, computed for the highest resolution simulation, are the same to within 10 per cent (Fig. 6, green and blue lines, respectively), even though the numerical time-scale displays oscillatory behaviour, due to the slight orbital eccentricity. This is the cause of the rapid oscillations visible in the bottom panel of Fig. 6. This means that the relationship between the change in stellar masses, angular momentum loss, and orbital separation are in line with the analytical prescription. Equation (2) assumes that both the stars are point masses, which is not true in our case. However, the small differences between the analytical and numerical time-scales suggest that the point mass approximation is still valid.

In Fig. 6, we also plot equation (2), but assuming that $\dot{J} = 0$ (dashed red line), or assuming that $\dot{M}_2 = -\dot{M}_1$ (dashed-dotted red line). For the case where $\dot{J} = 0$, \dot{a}/a is positive throughout, while if $\dot{M}_2 = -\dot{M}_1$, \dot{a}/a is mainly negative, and similar to the observed orbital decay. By separating the effect of mass transfer from the effect of angular momentum loss, we deduce that the decrease in orbital separation is primarily driven by the loss of angular momentum via L_2 and L_3 .

After the end of the Roche lobe overflow phase, at around 4600 d in the high-resolution simulation, the dynamic inspiral phase begins. At this time equation (2) can no longer be used to predict the time-scale accurately, because it becomes difficult to determine the stellar masses when they are orbiting within a common envelope. As a

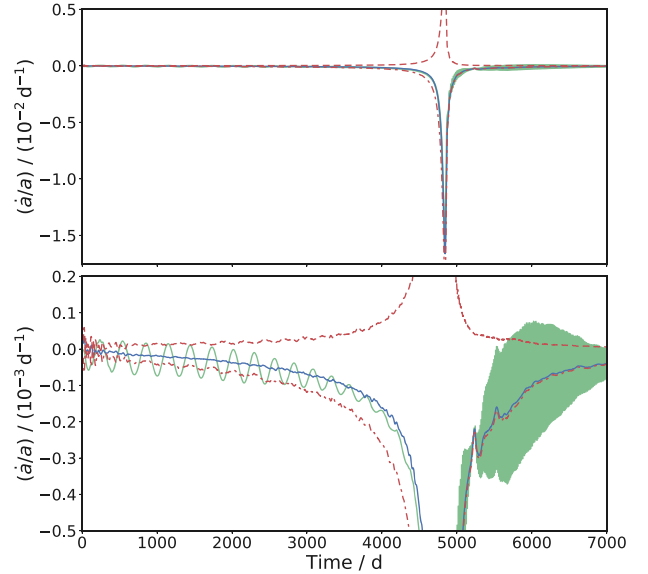


Figure 6. Comparison of the simulated orbital evolution time-scale (solid green line) for the 1.1 million SPH particle simulation, with the analytic time-scale computed from equation (2), solid blue line). Also displayed lines computed with equation (2) where we have set $\dot{J} = 0$ (dashed red line) or $\dot{M}_2 = -\dot{M}_1$ (dashed-dotted red line). The bottom panel is the same as the top panel, except with a truncated y-axis. The green block in the bottom panel is caused by rapid oscillations in the green line.

result, the time-scales do not match as closely as before the dynamic inspiral, although they still display the same basic behaviour.

We finally note that comparing \dot{a}/a using equation (2) to the numerically measured value is similar to the approach of MacLeod et al. (2018b). They reconstructed the full orbital evolution using a similar equation (see their fig. 10), obtaining good agreement with the simulated orbital evolution.

4.1.2 The mass transfer rate

We next investigate the mass transfer during the Roche lobe overflow phase and the ability of simulations to reproduce it. The aim is to determine whether the simulations can indicate the duration of the unstable Roche lobe overflow phase, and ultimately lead to a better determination of the criterion of instability.

For the simple case of a binary with a non-spinning giant donor, which can be modelled as a polytrope of index $n = 1.5$, and for which the mass transfer is perfectly conservative, unstable mass transfer occurs for $q \gtrsim \frac{2}{3}$ or 0.67 (Tout & Hall 1991). The mass ratio of our system is $q = 0.68$, our primary star starts with no spin, and is fairly well approximated by a polytrope of index $n = 1.5$ (suitable for red giant stars). However, our mass transfer is non-conservative. About 10 per cent of the donor mass is transferred during this phase, but only about 13 per cent of the transferred mass is retained in the potential well of the companion, with the remaining mass being lost from the binary system. It is therefore expected that our system should be unstable, as demonstrated by our simulations.

In Fig. 7, we plot the simulated mass transfer rate determined as described in Section 4.1.1. We truncate the lines to show the time span of interest, namely before the system enters the dynamic inspiral. As mentioned in Section 3.2, this time is chosen as the first point when $|\dot{a}/a| \geq \frac{1}{15} \max |\dot{a}/a|$. After this time (about 4600 d in

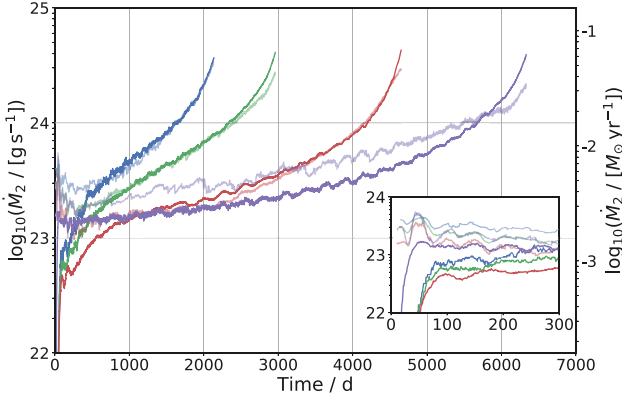


Figure 7. Mass transfer rate on to the companion as a function of time. As previously, blue, green, and red lines represent the low-, medium-, and high-resolution simulations, respectively, while the purple line is used for the medium-resolution simulation in a corotating frame. Darker lines are mass transfer rates measured from the simulations. Light lines represent the analytical form of the expected mass transfer rate given inputs from their respective simulations (see equation 3). Insert: detail of the first 300 d of the simulations.

the high-resolution simulation), the Roche geometry is no longer applicable and measuring mass transfer no longer makes sense.

As expected, the transfer of mass from the primary to the companion starts slowly (about $10^{22} \text{ g s}^{-1} = 1.6 \times 10^{-4} M_{\odot} \text{ yr}^{-1}$), and increases by two orders of magnitude as the orbital separation decreases. Because of the discretization of mass in SPH simulations, the minimum (non-zero) rate of mass transfer is when one SPH particle passes L_1 between two consecutive code dumps (dumps are approximately every 80 000 s). This corresponds to mass transfer rates of 10^{23} and 10^{22} g s^{-1} , for the lowest and highest resolutions we adopt, respectively. The measured mass transfer rate curves in Fig. 7 have been smoothed using a Savitzky–Golay filter with a width of 35 data points, showing the underlying trends in the mass transfer measurements (which can otherwise be noisy when close to the minimum rates), so the plotted rate can be smaller than the minimum simulated rate. We stress that this is a result of smoothing the curves, and no rate below the minimum can actually be measured. We can only consider the measured mass transfer rates after a simulation time of ~ 300 d, when the transfer rates, at all resolutions, are larger than the minimum measurable. At a time of 300 d mass transfer rates are quite similar for all resolutions, varying from 10^{23} g s^{-1} at our lowest resolution to $5 \times 10^{22} \text{ g s}^{-1}$ at the highest resolution.

A question is whether we can verify these mass transfer rates. An analytical expression for stable and conservative mass transfer rate through the L_1 point is that of Jędrzejec (Paczynski & Sienkiewicz 1972),

$$\dot{M}_1 = -S_1 \left(\frac{\mu m_{\text{H}}}{k_{\text{B}} T} \right)^{1.5} W(M_{1,\text{rel}}) \rho G^2 M_1^2 \left(\frac{\Delta R}{R_1} \right)^3, \quad (3)$$

where $S_1 \approx 0.215$ is a constant factor related to the polytropic index, μ is the mean molecular weight, m_{H} is the mass of a hydrogen atom, k_{B} is Boltzmann’s constant, T is the temperature at the photosphere of the donor, ρ is its photospheric density, G is the gravitational constant, M_1 is the mass of the primary, and $\Delta R = R_1 - R_{\text{L},1}$, where R_1 is the radius of the primary and $R_{\text{L},1}$ is its Roche lobe radius. The quantity $W(M_{1,\text{rel}})$ is a function of $M_{1,\text{rel}} = M_1/M_2$

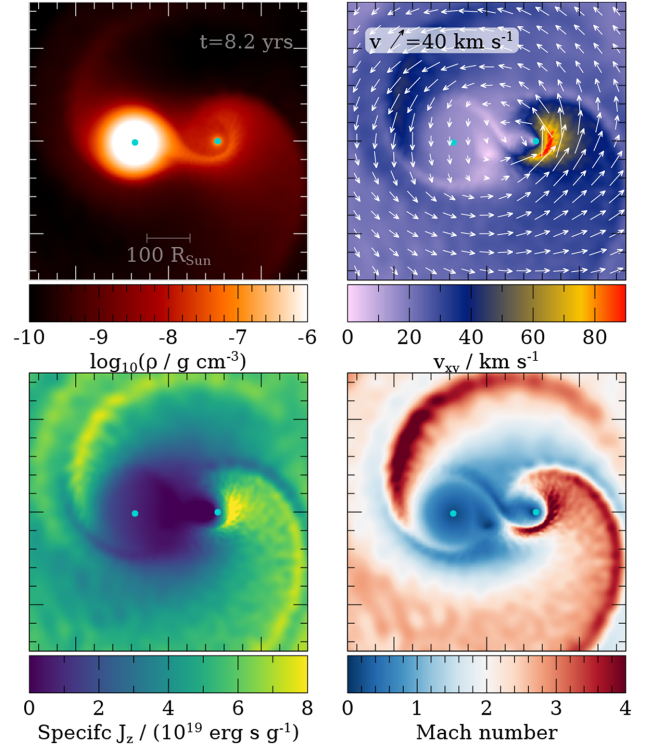


Figure 8. Slices showing detail of the mass transfer stream. The panels are rendered in density (top left), velocity (top right), angular momentum (bottom left), and Mach number (bottom right). The frames are 3 au on each side, and are taken at 8.2 yr, matching the second row of Fig. 2. Green dots represent the point mass cores.

+ M_2), defined as

$$W(M_{1,\text{rel}}) = \frac{\sqrt{M_{1,\text{rel}}} \sqrt{1 - M_{1,\text{rel}}}}{(\sqrt{M_{1,\text{rel}}} + \sqrt{1 - M_{1,\text{rel}}})^4} \left(\frac{a M_{1,\text{rel}}}{R_{\text{L},1}} \right)^{n+1.5}, \quad (4)$$

where a is the orbital separation and n is the polytropic index, taken to be 1.5 for a red giant. A similar derivation for \dot{M}_1 with an isothermal flow was made by Ritter (1988), although we use equation (3) because it is valid for adiabatic flows.

The mass transfer rate equation (3) applies to giant transferring mass conservatively. It assumes a system with a corotating primary star and that, as the mass flows through the L_1 point, it transitions from subsonic to supersonic. The first of these conditions is only true for one of our simulations. However, our simulations do have a sonic point between the two stars (see the bottom right panel of Fig. 8). With this in mind, we apply equation (3) to our simulations.

To determine the mass transfer rate from equation (3), we recognize first that the equation can be slightly simplified, when using an ideal equation of state, with the relation

$$\frac{P}{\rho} = \frac{k_{\text{B}} T}{\mu m_{\text{H}}}, \quad (5)$$

where P and ρ are the surface pressure and density of the star, respectively, as defined below. We make this change because pressure and density are quantities more easily recoverable from the simulation. When the star is distorted by the presence of the companion, it is not trivial to determine its radius. This difficulty is compounded by material filling the orbit after having been stripped from the primary during Roche lobe overflow. In this case, we found that the radius can be obtained by measuring the diameter of the

sphere along the z -axis, defined by the distance between particles with the greatest positive and negative z -coordinate and adding twice their respective smoothing lengths. Only particles with density lower than the initial surface density of the star were considered. By sampling the radius perpendicular to the orbital plane, we were able to obtain more reliable radius estimates than if we used the volume equivalent radius measurement mentioned in Section 2. The surface pressure and density were then determined by averaging these values over a sphere with the stellar radius determined in this way.

The analytical form of the mass transfer rate (equation 3) is compared with the measured numerical rate in Fig. 7 for the high-, intermediate-, and low-resolution simulations (red, green, and blue lines, respectively) and for the simulation carried out in the corotating frame (purple line). We plot the numerical and analytical mass transfer rates with dark and light colours, respectively.

The analytical mass transfer rate is slightly higher than the numerical rate at 300 d, our fiducial start of the simulation as described above, but the difference is smaller for higher resolutions. This initial difference is due to the fact that equation (3) represents instantaneous mass transfer rates, and the simulations require some time to begin mass transfer. Both the simulations and the analytical approximation indicate that the mass transfer rate should increase in time, changing by 1–2 orders of magnitude over the course of the simulation. Finally, the analytical mass transfer rate is slightly lower at the end of each simulation when compared to the numerical form. Considering the imprecision with which we define the stellar radius and the third power dependence of the mass transfer rate on that number, the discrepancy between numerical and analytical approaches here is reasonable, and lends credence both to our results and to equation (3).

A similar comparison was carried out by MacLeod et al. (2018b, e.g. see their equation 1 and fig. 7). They achieved a close match between the analytical and numerical mass transfer rates using a simplified version of equation (3). The fact that two independent simulation codes obtain good fits to similar equations, provides excellent code verification and suggests that the equation itself provides a good physical approximation.

4.1.3 The decretion disc

As mentioned in Section 4.1.1, gas is ejected during Roche lobe overflow from L_2 , and later at L_3 , forming a spiral pattern (Fig. 8). From our high-resolution simulation we estimate that, over the course of the Roche lobe overflow phase, this outflow carries approximately 9×10^{51} erg s of angular momentum away from the binary (23 percent of the total angular momentum budget of 3.87×10^{52} erg s) and about $7.8 \times 10^{-2} M_{\odot}$, driving the decrease in the orbital separation. The arms of the spiral outflow eventually coalesce at about $2000 R_{\odot}$ from the central binary, forming a decretion disc. The decretion disc is contained within approximately $5000 R_{\odot}$ from the centre of the binary (see Fig. 9). Within the disc, the range of smoothing lengths h is about 30–1000 R_{\odot} . Approximately $1.5 \times 10^{-3} M_{\odot}$ of gas lies outside $5000 R_{\odot}$ and contains gas unbound from the system within the first year of the simulation.

By considering the outward moving, but bound disc gas to be in a ballistic trajectory and using conservation of energy and angular momentum, we determine the radius and time-scale of formation of a Keplerian disc around the binary (Tocknell, De Marco & Wardle 2014). We calculate a specific angular momentum for the disc gas

of 5.8×10^{19} erg s g^{-1} and find that this bound gas would fall back to form a Keplerian, circumbinary disc with a radius of about $130 R_{\odot}$ from the centre of mass. This is well outside the final orbital separation of the system. The time taken for this trajectory would be at least 20 yr. However, in our simulation, the L_2 and L_3 outflow structure is unlikely to survive for long enough to fall back into a Keplerian circumbinary disc, because the denser, faster gas outflow promoted by the early inspiral quickly overtakes the lighter expanding structure. This said, a longer Roche lobe overflow phase that ejects more mass followed by a weaker common envelope ejection could possibly result in the survival of a circumbinary disc with a radius on the order of a few hundred solar radii. We discuss this further in Section 5.1.

4.2 The dynamical inspiral phase

At some stage in a common envelope interaction, the orbital separation starts to decrease at a faster rate. This occurs in our high-resolution simulation at approximately 4600 d, as indicated by the time-scale of the system (Fig. 6). At this point, the mass transfer is no longer characterized by the mechanism of Roche lobe overflow because the system is no longer described accurately by the Roche geometry.

As the companion splashes into the atmosphere of the primary (13.3 yr into the high-resolution simulation), it unbinds a shell of material which travels outwards at speeds of about 40 km s^{-1} . This event is visible in the fourth row of Fig. 2 (at 13.8 yr), and later on as the shell has travelled outwards at 13.8 yr, it is located at approximately $1000 R_{\odot}$ from the binary at the centre. We can also see in the perpendicular plane (far right column in Fig. 2) at 13.8 yr how the material expands more rapidly above and below the orbital plane, while the material in the orbital plane encounters the L_2 and L_3 outflow material and decelerates. This effect is similar to what is observed in the simulations of MacLeod et al. (2018a, e.g. see their section 6).

The binary has entered a common envelope and the inspiral is now driven primarily by gravitational drag forces. While hydrodynamic drag is the force felt by a body owing to direct collisions between the body and the particles of the ambient medium through which it is moving, gravitational drag operates purely through gravitational interactions between the gas and the core particles. Hydrodynamic drag tends to be insignificant in typical binary common envelope interactions, though for lighter companions, such as planets, it can be relatively more important due to a smaller gravitational drag (Staff et al. 2016b). We can only simulate gravitational drag, because the point mass particles have no physical size. This said, gas tends to collect in the shallow potential wells around point masses and travels with them, something that does effectively give them a radius. However, any collisions between the ambient medium and the material in the potential wells still only affect the cores via gravitational interactions.

4.2.1 The simulated and analytical strength of the gravitational drag

While one could expect that the strength of the drag is affected by resolution, it has been shown previously (e.g. Passy et al. 2012; Iaconi et al. 2017) that it is only marginally so. This means that resolution does not dramatically affect the final separation or the speed of the inspiral (we can appreciate this by looking at Table 2). Staff et al. (2016b) showed that in the case of their interaction

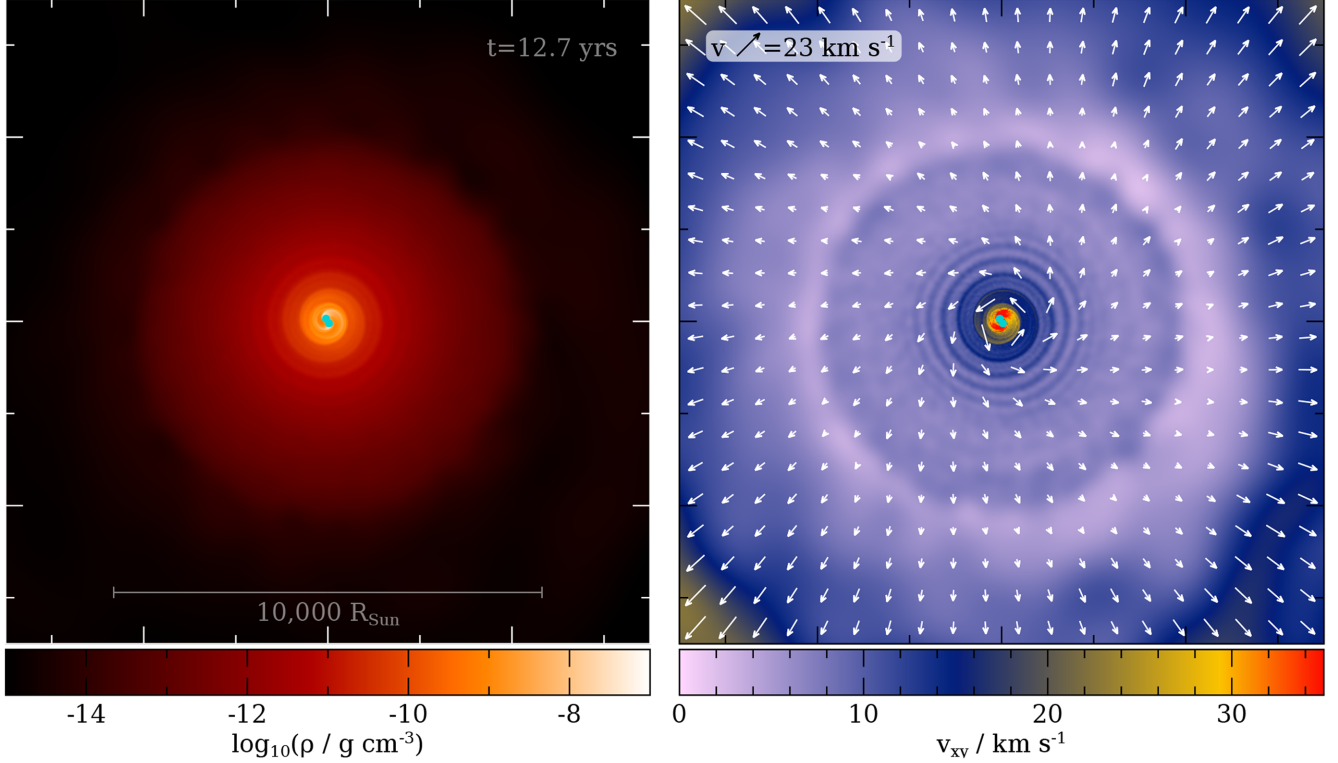


Figure 9. Cross-sections of density (left) and velocity (right) in the orbital plane of the excretion disc at the beginning of the dynamic inspiral, at 12.8 yr, for the 1.1 million particle simulation. These frames are taken at the same time as the third row of Fig. 2 (12.8 yr), but are zoomed-out such that the frames are 70 au per side. The green dots represent the cores.

with a planetary mass companion, the strength of the gravitational drag was commensurate with that determined by an analytical approximation. Here, we carry out a similar comparison for our stellar-mass companion. Below we compare the drag calculated in three distinct ways, two from the simulations directly and one using an analytical prescription together with simulation quantities, as done before.

The physical parameters that influence the gravitational drag are the mass of the embedded body, the density of the surrounding fluid, and the velocity contrast of the body and the fluid. In a common envelope, however, there may be additional factors playing a role, such as the density gradient (MacLeod et al. 2017b).

The gravitational drag has been represented by several authors, with some variability of form (e.g. see Shima et al. 1985), as

$$F_{\text{drag}} \approx \xi \pi R_a^2 \rho v_{\text{rel}}^2, \quad (6)$$

where ξ is a factor dependent on the Mach number, $R_a = 2GM_2/(v_{\text{rel}}^2 + c_s^2)$ is the accretion radius, M_2 is the mass of the companion, c_s is the local sound speed, ρ is the density around the particle, and v_{rel} is the relative velocity of the core and the surrounding gas. The parameter ξ is greater than 2 for supersonic motion and less than 1 for subsonic motion (Shima et al. 1985) but, owing to difficulties in calculating this quantity on the fly, it is typically just held at unity.

We use equation (6) as a comparison to the numerical drag forces measured in our simulation with the knowledge that the expression itself may have only limited validity in our situation. To use this expression, we need to derive from the simulations the relative velocity of the companion and the density of surrounding material.

To calculate these quantities we need to define a spherical volume around the companion. In this case, the radius we use is the distance from the companion particle to the centre of mass of the orbit. This distance varies from about $100 R_\odot$ to about $10 R_\odot$ as the orbit shrinks. The mean velocity vector of the gas in this volume is then projected on to the velocity vector of the companion, and the difference is found. The average density is similarly found within the same volume.

An alternative method is to use a spherical volume with a constant radius, such as the $20 R_\odot$ used by Iaconi et al. (2017). The radius cannot be too small or else only the material caught in the potential well of the companion would be included (this material has a low velocity contrast and a high density) and cannot be too large or else during the late inspiral the core of the primary would be included. Both methods have their benefits but, within the timespan of the dynamic inspiral in our simulations, we find using a variable volume to be superior.

Finally, equation (6) assumes a homogeneous medium, which is not the case in our simulations. In a common envelope, there is a relatively strong density gradient perpendicular to the companion's velocity, along with an overdensity caught in its potential well. Therefore, the output of equation (6) should be taken as indicative.

There are two ways to calculate the drag force directly from the simulations. The first is via the change in angular momentum J of the point mass particles, with respect to the centre of mass by

$$F_{\text{drag}} = \frac{j}{r}, \quad (7)$$

where r is the distance of the companion from the centre of mass. It should be noted that this only takes into account the component

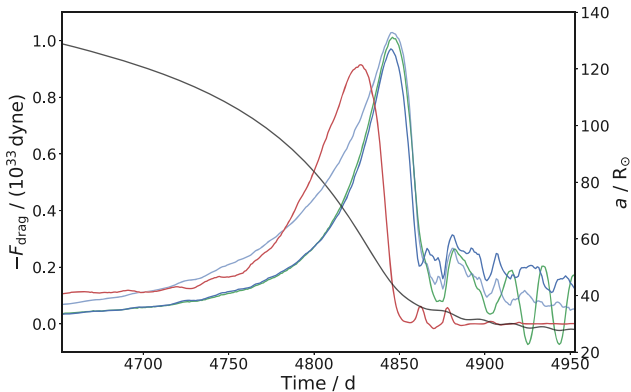


Figure 10. Gravitational drag force on the companion in the 1.1 million particle simulation, calculated with different approximations: by summing gravitational interactions with gas particles in the full computational domain (dark blue line) or in a spherical volume with a radius extending from the companion to the centre of mass (light blue line); by the measured loss of angular momentum from the orbit [green line; equation (7)] or by the analytical form of the drag force [red line; equation (6)]. The orbital separation is plotted in black. We restrict the plot to the time over which the system is undergoing fast inspiral.

of the drag which is perpendicular to the radius from the centre of the orbit. Hence, if the orbit is not circular, this equation yields a lower limit for the drag force. For our case, the very small departure from zero eccentricity makes this expression accurate to within one per cent (the angle between the velocity vector and tangent of the circular orbit varies between 0 and 8 deg over course of the simulation).

The second way to determine the dynamical friction in a simulation is to calculate directly the net force experienced by the companion as a result of the surrounding gas. If the gas around the companion was spherically symmetric then there would be no net force acting on the companion particle. However, owing to the motion of the particle through the gas, the symmetry is broken by a high-density wake that forms behind the companion. To calculate this force, we add up the gravitational forces between the companion and a set of gas particles. This total force is then projected on to the velocity vector of the companion to give the dynamical friction of the gas on the companion particle. When comparing the two numerical approaches, we sum up contributions from all particles in the computational domain. However, in order to make an honest comparison with equation (6), which estimates local drag forces, we instead use only the subset of gas particles residing in the same volume around the companion that we used for the analytical approximation.

The analytical and numerical forces are plotted in Fig. 10, where the force is negative because it acts in the opposite direction to the orbital motion. Here, we see that the drag force calculated by the change in angular momentum (green curve) is almost identical to the force derived by direct summation, as long as the contributions of all particles are included (dark blue curve). If, on the other hand, we calculate the drag force by direct summation but using only the previously defined subset of particles (light blue curve), then the drag force is stronger right up until the peak. This comparison therefore implies that the gravitational drag is not entirely a local phenomenon, with gas outside the immediate vicinity of the companion serving to mitigate the strength of the drag.

The peak of the analytical force (red curve in Fig. 10) leads by ~ 20 d the peak of the numerically derived force. The reason for this is that any method that averages quantities within a volume around the companion includes substantial stationary gas caught in its potential well. This decreases the average velocity contrast while increasing the density, something that overall decreases the strength of the analytically derived force (though we note that the peak strength is within 10 per cent of the numerical value). This is particularly so at a time when the sampling volume around the companion is becoming smaller because of the orbital shrinkage, something that leads to a premature decrease in the analytical force, leaving the peak shifted to an earlier time compared to the numerical calculations. If the volume instead has a constant radius of $30 R_{\odot}$, then the peak of the analytical force coincides with the numerical result, but the peak force is stronger by about a factor of two compared to the numerical values. Also worth mentioning is the parameter ξ in equation (6), which is dependent on the Mach number, and may vary the analytical drag force by a factor of order unity. We suggest that, when analysing common envelope interactions, equation (6) should only be used to approximate the magnitude of the drag force.

4.3 The orbital stabilization phase

The orbit of the two cores stabilizes at around $30 R_{\odot}$, independent of resolution. By the end of the high-resolution simulation, the rate of decrease of the orbit has slowed down to about $0.5 R_{\odot} \text{ yr}^{-1}$, though this descent is still decelerating.

In Fig. 10, we see that at some point there is a significant reduction of the drag force. The cause of this lower force is not so much the lower density of the surrounding gas, but rather that the gas has been dragged into corotation. Fig. 11 shows two snapshots from the high-resolution simulation, showing two cross-section slices of the quantity $(\omega_{\text{gas}} - \omega_{\text{bin}})/\omega_{\text{bin}}$, where ω_{gas} and ω_{bin} are the angular velocities of the gas and the binary around the centre of mass, respectively. The left-hand panel shows the time when $|\frac{a}{a}|$ is a maximum, corresponding to the maximum rate of inspiral, while the right-hand panel shows the same quantities a few months later, at the end of the dynamical inspiral. The gas surrounding the cores is rotating more uniformly in the second panel and it is in approximate corotation, preventing the cores from losing further angular momentum to the envelope gas. This feature can also be seen in Fig. 5, in which the angular momentum carried by the point mass particles remains approximately constant after the end of the dynamical inspiral.

What follows is complex and depends on how much of the envelope is unbound. Stellar structure theory dictates that for a giant star to depart from the giant branch and shrink, all but a very small amount of envelope must be lost. If the envelope is merely lifted by the common envelope inspiral, but not unbound, the orbit may stabilize while it has little gas within it. We could expect that if the envelope is ejected and the star departs the giant branch shrinking to within its Roche lobe, a small part of the envelope that was lifted but not ejected would return to form a low-mass circumbinary disc. However, if the majority of the lifted envelope is not ejected, then a substantial amount of mass would return to the binary, resulting in a further interaction.

The time-scale of this return could be very small, though the ballistic calculation of Kuruwita, Staff & De Marco (2016) is only a lower limit because it does not account for gas pressure. Ultimately, this question cannot be answered while we do not have

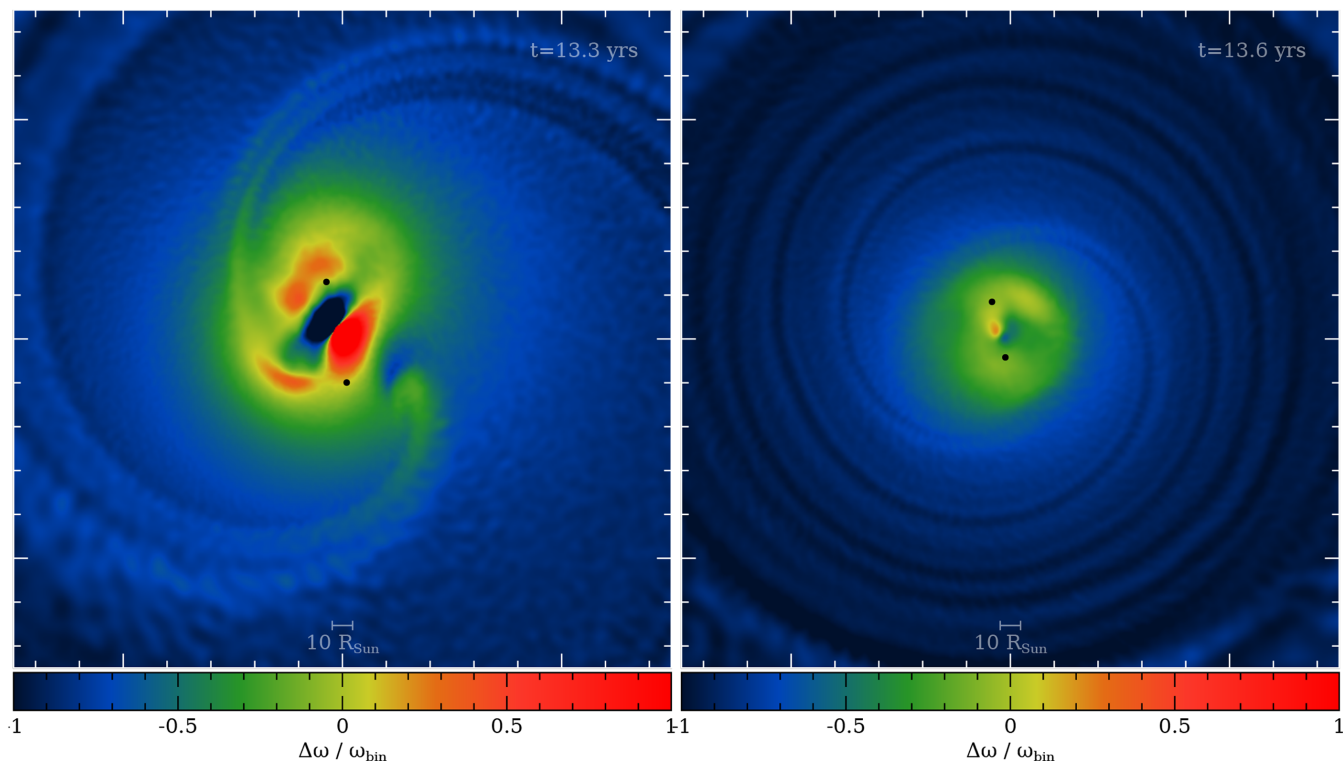


Figure 11. Slices in the XY -plane of the 1.1 million particle simulation, rendering the quantity $\Delta\omega/\omega_{\text{bin}}$, where $\Delta\omega \equiv \omega_{\text{bin}} - \omega_{\text{gas}}$, and ω_{bin} and ω_{gas} are the angular velocity of the point masses and the gas, respectively. The two snapshots are taken when the system is experiencing the most rapid reduction in orbital separation (left), and at the end of the dynamic inspiral (right). The frames have a side length of 1.5 au. Black dots represent the point masses.

a definitive answer to the energetics of the envelope and under what circumstances it may be unbound.

4.4 Common envelope fallback

If most of the envelope is still bound after orbital stabilization, we expect it to fallback rapidly. There are several effects which can lead to envelope ejection at the end of the common envelope phase. Soker (2017) discuss these processes, suggesting that jets may play a major role in envelope removal both at the beginning and end of the interaction. Further, simulations that use a non-ideal equation of state, including the contributions of ionization and recombination, have tended to unbind much more of the envelope than those, such as ours, that use an ideal equation of state (Nandez et al. 2015). It is likely that, had our simulations included recombination energy, they would be placed among the simulations that succeed in fully unbinding the entire envelope (Iaconi et al. 2018). However, even leaving aside the controversy of how much recombination energy can be used to unbind the envelope (Ivanova 2018; Soker et al. 2018), there are situations where the envelope would not be fully unbound even with recombination energy, such as those with initial masses $\gtrsim 2 M_{\odot}$ (Nandez & Ivanova 2016). In these cases, substantial mass would fallback, so it is worth expending a few words on common envelope fallback gas.

Kuruwita et al. (2016) investigated how the bound part of the common envelope returns and whether it should form a disc thanks to the added angular momentum. They could not follow the entire outward and return journey of the gas, but using their set-up they

could deduce that gas would return in a matter of months to a few years, and that much of this gas would return all the way to the core. However, their calculation did not account for the fact that gas, upon returning, collides with outflowing gas. Since SPH allows us to track envelope material far from the central binary, we can investigate the dynamics of this gas over a longer time-scale. This allows us to take another look at the idea of an envelope fallback event, beyond what was done by Kuruwita et al. (2016).

We consider SPH particles to be falling back if they have a negative radial velocity component with respect to the centre of mass and if they are located outside of a spherical volume encompassing the two stars. The total mass (blue line), angular momentum (red line), and the mean radial velocity (green line) of these particles are plotted in Fig. 12. Before the dynamic inspiral, there is very little material meeting our fallback criterion, as expected. During the inspiral, material is very rapidly evacuated from the region around the binary, catching up, and colliding with material that was ejected previously. However, at the end of inspiral this evacuation stops and the material is able to fallback on to the central binary. The distribution of fallback mass is shown in Fig. 13, and can be seen to be approximately circular at larger radii.

None of this fallback material returns to the vicinity of the binary. Instead it collides with more gas, flowing out from the region around the binary. It is possible that the region immediately surrounding the binary would become almost completely evacuated at some point, allowing future fallback material to return to the very inner portions of the system. However, we have not been able to follow the simulation for long enough to see this.

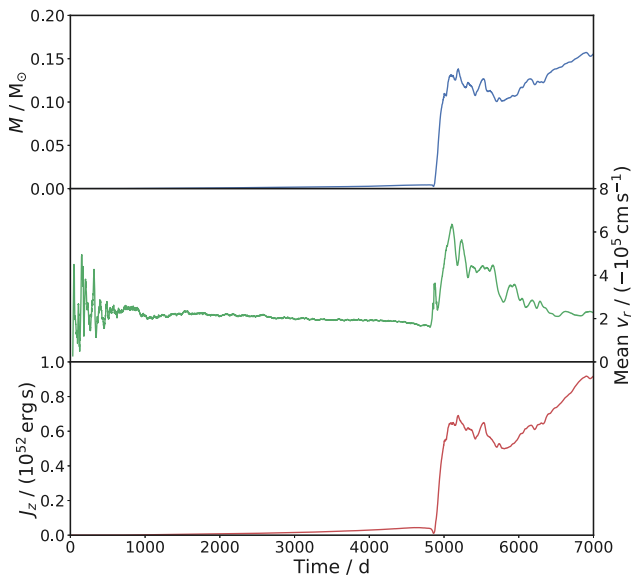


Figure 12. Fallback mass (upper panel), the average radial velocity of this mass (middle panel), and the angular momentum of this mass (lower panel) as functions of time.

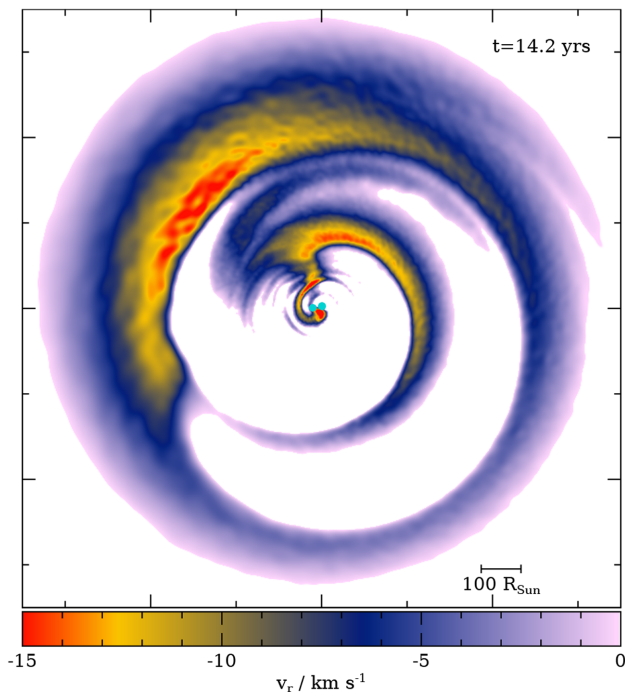


Figure 13. Distribution of gas displaying a negative radial velocity at $t = 5188$ d for the 1.1 million particle simulation, when the largest amount of fallback mass was present in the simulation. Material is rendered by its *negative* radial velocity value. Material with a positive radial velocity is not rendered. The frame is 7 au on each side.

5 PLANETARY NEBULAE AND THE SHAPE OF THE COMMON ENVELOPE

At least one in five PNe are ejected common envelopes (Miszalski et al. 2009), and the symmetry axis of post-common envelope PNe with well-characterized binaries can be shown to align with the orbital axis (Hillwig et al. 2016). The shapes of the approximately

40 known post-common envelope PNe are interestingly inhomogeneous, although some common features, such as bipolarity, are observed in many cases (De Marco & Soker 2011). However, there is ultimately no obvious set of features that identifies the origin of a given PN as deriving from a common envelope interaction.

PNe derive their shapes from the interaction of the fast and tenuous post-asymptotic giant branch (AGB) wind with a previous slow and massive AGB wind (Balick & Frank 2002). The AGB slow wind creates a mould into which the fast wind expands. The common envelope provides gas distributions with an equatorial density enhancement. Such distributions are relatively small and dense compared to those generated by a slower mass-loss process. It is useful to determine the key differences between PN generated from post-common envelope distributions and those generated by single stars or other binary phenomena.

García-Segura et al. (2018) have recently demonstrated how a common envelope density distribution, generated by the simulation of Ricker & Taam (2012), can lead to a bipolar PN. They mapped the gas distribution at the end of common envelope simulation of Ricker & Taam (2012) into a 2D plane, where only a quarter of the domain was simulated assuming two axes of symmetry, one along the orbital plane and one perpendicular to it. The input gas distribution from the common envelope simulation was taken after 56.7 d of common envelope evolution, when the binary separation between the $0.36 M_{\odot}$ degenerate core and $0.6 M_{\odot}$ companion was approximately $9 R_{\odot}$. A further $0.69 M_{\odot}$ of gas mass is in the ejected envelope. García-Segura et al. (2018) modelled the central binary as a point with an effective temperature of 29 000 K, corresponding to a star with a wind velocity of 600 km s^{-1} (though they also performed two simulations with faster and slower winds). By evolving their simulation for 10^4 yr, they demonstrated that forming a bipolar nebula is, as predicted, a natural consequence of blowing a spherical wind into a toroidal gas distribution. Their simulations offer compelling evidence that connecting the common envelope with bipolar nebulae is a path certainly worth further study.

Frank et al. (2018) used instead the simulation described here as a starting point for a PN simulation. Below we give further information as to the shape of the common envelope into which the post-AGB fast wind expands and compare their work further to that of García-Segura et al. (2018).

5.1 The common envelope's gas distribution at the onset of the post-AGB fast wind

The binary star considered by our simulation differs from that of Ricker & Taam (2012). Our primary star is a $0.88 M_{\odot}$ giant with a $93 R_{\odot}$ radius, while they used a $1.05 M_{\odot}$ giant with a $31 R_{\odot}$ radius. Therefore, their giant is more bound and is more similar to a less evolved, more compact RGB star than the more extended AGB stars that form PNe. The more bound nature of their giant leads to a faster evolution over all and a more compact, denser common envelope ejection. Additionally, we evolved our simulation for longer, particularly before the dynamic inspiral. Despite the fact that both simulations start with the companion near the beginning of Roche lobe overflow, our simulation spends a much longer time before the dynamic inspiral, and more gas is launched out of the L_2 and L_3 points before the common envelope ejection takes place. This provides us with a more extended common envelope gas distribution into which the post-AGB wind expands.

In addition, the shape of the extended common envelope is greatly influenced by the interaction of the Roche lobe overflow with the outflow from the common envelope inspiral. During the Roche lobe

overflow phase, gas leaves the system primarily through L_2 and L_3 (see Fig. 2). There is almost no unbinding of material in this phase (Fig. 3). The following outflow during the fast inspiral phase interacts with the Roche lobe overflow ejecta. This gas distribution, shown both in the final row of Fig. 2 and in the top and middle frames of Fig. 14, is toroidal. The polar regions in the distribution are approximately one to two orders of magnitude less dense than the material immediately surrounding it on the equatorial plane. The velocities of the ejecta are also considerably greater in a direction perpendicular to the orbital plane. Hence, the relative difference in density continues to increase as the distribution expands.

The bottom row of Fig. 14 shows a slice of a simulation identical to those we have presented here, except that the initial orbital separation was set to $100 R_\odot$ (instead of $218 R_\odot$). For more details on that simulation, see Iaconi et al. (2017). All of the slices in Fig. 14 are produced at 1000 d after the beginning of the fast inspiral in their respective simulations. By comparing the middle and bottom row panels, we see that the gas distributions depend heavily on whether the pre-inspiral phase was simulated or not. The bottom row frames show that there is a large lobe to the right of the frame, which is rapidly expanding. There is a hint of the funnel regions of low density above and below the orbital plane but it is certainly not as distinct as the middle panels. The initial orbital separation, the length of Roche lobe overflow phase, the condition of the primary as a rotating or non-rotating star, all make a difference to the shape and degree of symmetry of the ejecta. The best PN simulations will therefore result from common envelope simulations that account for as complete an interaction as possible.

The Roche lobe overflow phase does however appear to have an especially prominent effect in promoting symmetry in the final distribution. We therefore suggest that the amount of mass loss before the inspiral makes a difference to the shape of the ensuing PN. We also predict that differences in the nebular shape are the result of more or less stable pre-common envelope mass transfer, likely induced by a larger or smaller companion mass.

5.2 The SPH-AMR PN simulation

In our high-resolution simulation, all particles have an equal mass of $4.54 \times 10^{-7} M_\odot$. Typical post-AGB winds release mass on the order of $10^{-8} M_\odot \text{ yr}^{-1}$. As PHANTOM currently does not support unequal mass particles, we are unable to model both the common envelope and the spherical wind in the same simulation. The 3D post-common envelope gas distribution has therefore been mapped into a series of nested grids using SPLASH (Price 2007) and used as input to the 3D AMR grid code ASTROBEAR (Cunningham et al. 2011). Preliminary results of this PN simulation have been presented by Frank et al. (2018).

In summary, the ASTROBEAR domain is $16000 R_\odot^2 \times 128000 R_\odot$ in size, mapped with seven levels of refinement. Two spherical wind cases are simulated. In one, a spherical wind with a mass-loss rate of $6.4 \times 10^{-4} M_\odot \text{ yr}^{-1}$ is injected after a quiescent period of 500 d, while in the other a $3.2 \times 10^{-5} M_\odot \text{ yr}^{-1}$ mass-loss rate spherical wind is injected after a quiescent period of 6000 d. Both winds have speeds of 300 km s^{-1} . The simulations are each only run for approximately 1000 d after the injection of the wind, which is much less than for the simulations of García-Segura et al. (2018). A $46.9 R_\odot$, $1 M_\odot$ object is placed at the centre of the grid, replacing the binary, and the wind is blown from the surface of this object. This mass is also the only source of gravity in the simulation; no self-gravity is applied. Strong hydrodynamic collimation occurs in both these simulations, as in the simulation of García-Segura et al.

(2018), due to the narrow, evacuated funnel that can be observed in Fig. 14, upper left frame. We also note that the simulations of Frank et al. (2018) with the lower wind momentum display a strong degree of asymmetry between the upper and lower collimated lobes, with one much smaller than the other. This asymmetry could be a key to explaining objects such as the nebula around OH 231.8 + 4.2 (Meakin et al. 2003).

These are early days for hybrid common envelope PN simulations such as these, especially because neither of the two sets of simulations by García-Segura et al. (2018) or Frank et al. (2018) have used a common envelope gas distribution that is unbound. This means that the envelope velocity field is likely not properly reproduced.

6 SUMMARY AND CONCLUSIONS

We have presented a set of hydrodynamic simulations of the common envelope interaction aimed at extending the purely dynamical inspiral phase to include the previous, Roche lobe overflow phase as well as part of the post-inspiral phase. We also considered the post-common envelope, nebular phase. These simulations were carried out with the newly released SPH code, PHANTOM, and are based on an initial model of a $0.88 M_\odot$, RGB primary star with a radius of about $90 R_\odot$, and a $0.6 M_\odot$ companion (Passy et al. 2012), placed at an initial orbital separation of $218 R_\odot$, which is tuned to trigger Roche lobe overflow. Our main results are the following:

(i) Our *unstable Roche lobe overflow* lasts for a short time (between 6.4 and 12.7 yr, depending on resolution and 18 yr if the giant is corotating with the orbit). From trends with primary star rotation, stability, and resolution, we conclude that, in nature, this phase should last longer. Although we are unable to ascertain the length of the time between the onset of Roche lobe overflow and the fast inspiral with any certainty, we exclude that the phase during which mass loss is significant is longer than a few centuries for binary parameters similar to those we have modelled. Although this needs to be better quantified, mass loss should be deemed ‘significant’ when the material ejected prior to the dynamical inspiral makes a difference to the densities and kinematics of the circumstellar environment as a whole.

(ii) By examining the ejection of mass and angular momentum, we are able to see that the orbital evolution of the system responds in a way that is expected analytically to within a factor of a few. This shows that most of the pre-common envelope inspiral is driven by ejection of angular momentum via the outer Lagrangian points, L_2 and L_3 .

(iii) The flow ejected via L_2 and L_3 remains mostly bound: only $10^{-3} M_\odot$ are unbound with a further $7.8 \times 10^{-2} M_\odot$ remaining bound. If unobstructed, fallback of this material would form a disc at a radius of about $130 R_\odot$ on a time-scale of at least 20 yr. In our case, the unbound outflow associated with the subsequent dynamic inspiral disrupts this structure, in a manner similarly observed by MacLeod et al. (2018a). However, it is possible that, if the L_2/L_3 outflow phase were longer (mass transfer more stable), it may be followed by a weaker common envelope ejection, so that the disc structure formed during Roche lobe overflow may remain to become a long-lived circumbinary disc, such as those that have been observed around post-AGB binaries with periods between 100 and 1500 d (van Winckel et al. 2009).

(iv) Pejcha et al. (2016) simulated an L_2 flow in a binary that was not allowed to change its orbital separation. While they concluded that the L_2 outflow becomes unbound for mass ratios (accretor and

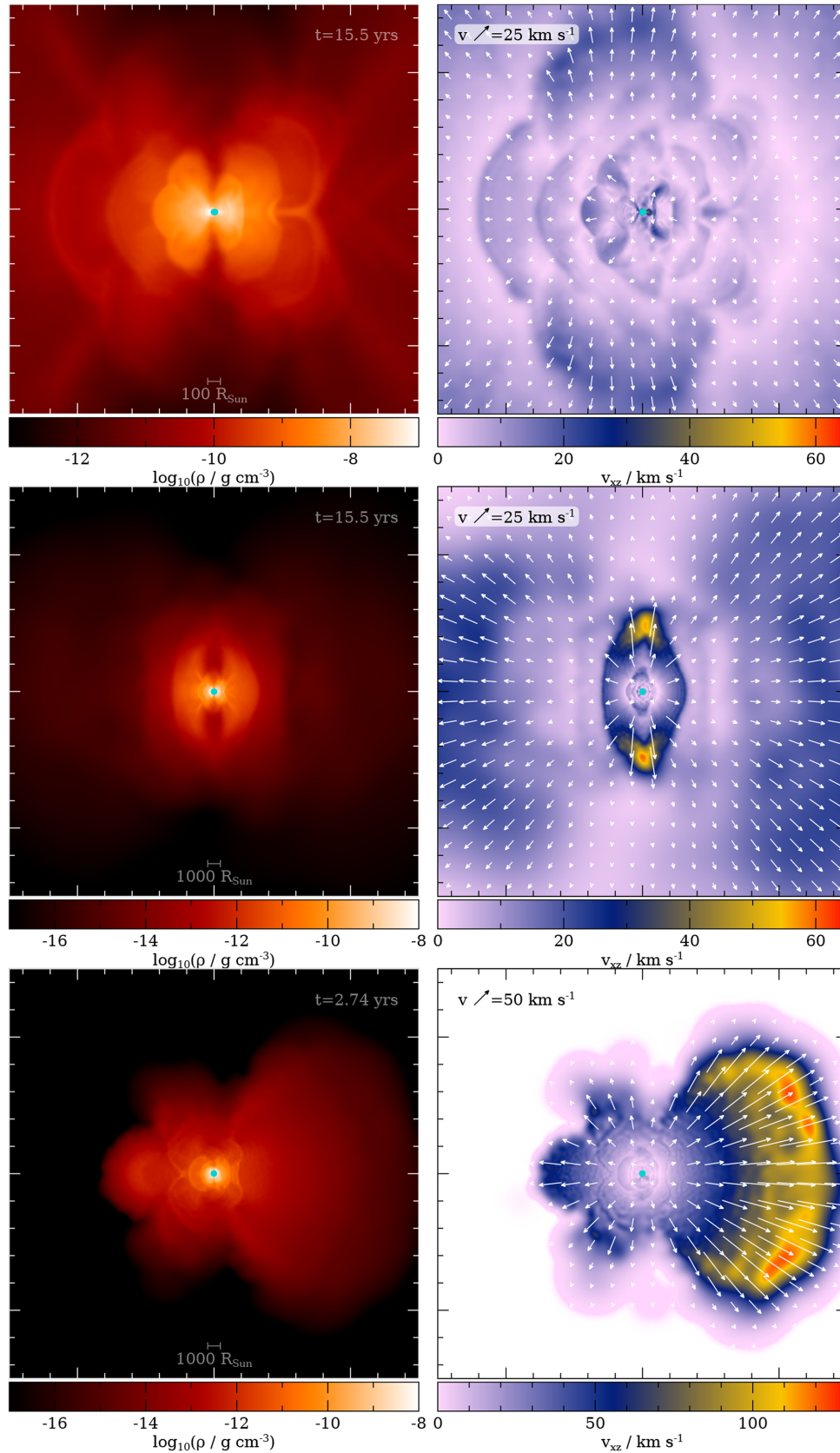


Figure 14. All frames are slices in the XZ -plane, rendered in density (left-hand column) and velocity (right-hand column). Top and middle rows display the our 1.1 million particle simulation from this paper, and differ by the scale: 15 au per side for the top row and 150 au for the middle row. The bottom row displays a simulation started with a smaller orbital separation of $100 R_{\odot}$, but that is otherwise identical, and has side length of 150 au to match the middle row. Note the different scales of the colour bars.

donor) in the range 0.06–0.8, this is at odds with both the results of our simulations and those of MacLeod et al. (2018a).

(v) The gravitational drag felt by the cores during the fast inspiral is within a factor of two of that calculated analytically using quantities from the simulation, as was also concluded for planetary mass companions by Staff et al. (2016b). This consistency exists despite the many approximations and assumptions and it increases our confidence in the inspiral time-scale being a reasonable approximation of reality. The *end of the inspiral* is brought about by gas being brought into corotation with the binary orbital motion. The gravitational drag is primarily local to the companion, but there is a contribution of the gas farther afield, which tends to mitigate the strength of the drag.

(vi) The low-, medium-, and high-resolution simulations unbind 33, 16, and 11 per cent of the gas mass, respectively (calculated without including internal energy). Hence, there is a trend to unbind less mass as resolution increases (Iaconi et al. 2017). Without having stabilized the star in the corotating frame, we are unable to definitively state what effect a rotating star has on the amount of unbound mass.

(vii) During the early stages of the *self-regulated inspiral* following the dynamic inspiral, as much as 30 per cent of the gas displays negative radial velocities. This fallback material is typically within $500 R_{\odot}$ of the central binary though, if the simulations were to be run for longer, material at larger radii would start to fallback too.

(viii) *The final gas distribution of our simulation is toroidal*, displaying a strong density contrast between the orbital plane and the polar directions. The common envelope ejection following the disc formation develops high velocities in the direction perpendicular to the orbital plane. However, this perpendicular ejection contains relatively little mass. It is not this mass that becomes visible as a bipolar PN later on. The highly evacuated polar funnels provide strong density contrast and powerful hydrodynamic collimation for the subsequence phase: the rarefied, fast wind from the heating post-AGB star (the core of the giant). This post-AGB ejection was simulated by Frank et al. (2018) using the density structure that is an output of this simulation.

(ix) By comparing our simulation to one where the companion was initially placed at the giant’s surface, and in which the dynamic inspiral develops immediately, suggests that simulating the Roche lobe overflow phase results in a far more symmetric distribution of gas, due to the regulating effect of the disc on the subsequent morphology. This is something that would impact the shape of subsequent PNe. This in turn suggests that the length of the Roche lobe overflow phase or, in other words, the degree of stability of the mass transfer, may explain the range of PN shapes of common envelope PN.

ACKNOWLEDGEMENTS

TR acknowledges financial support through the Macquarie University Research Excellence scholarship associated with Future Fellowship grant to O. De Marco (FT120100452). OD and DP acknowledge financial support through the Australian Research Council Future Fellowship scheme (FT120100452 and FT130100034, respectively). CAT thanks Churchill College for his fellowship and Macquarie University for supporting a visit. This work was supported by access to the swinSTAR supercomputing facility at Swinburne University of Technology. We finally acknowledge this paper’s referee, Morgan MacLeod for a helpful and constructive review.

REFERENCES

- Abbott B. P. et al., 2016, *Phys. Rev. Lett.*, 116, 061102
 Balick B., Frank A., 2002, *ARA&A*, 40, 439
 Blagorodnova N. et al., 2017, *ApJ*, 834, 107
 Bond H. E. et al., 2003, *Nature*, 422, 405
 Cunningham A. J., Frank A., Varniere P., Mitran S., Jones T. W., 2011, Astrophysical Source Code Library, record [ascl:1104.002](https://ascl.net/1104.002)
 De Marco O., Izzard R. G., 2017, *PASA*, 34, e001
 De Marco O., Soker N., 2011, *PASP*, 123, 402
 Eggleton P. P., 1983, *ApJ*, 268, 368
 Frank A., Chen Z., Reichardt T., De Marco O., Blackman E., Nordhaus J., 2018, *Galaxies*, 6, 113
 Galaviz P., De Marco O., Passy J.-C., Staff J. E., Iaconi R., 2017, *ApJS*, 229, 36
 García-Segura G., Ricker P. M., Taam R. E., 2018, *ApJ*, 860, 19
 Grichener A., Sabach E., Soker N., 2018, *MNRAS*, 478, 1818
 Han Z., Podsiadlowski P., Eggleton P. P., 1994, *MNRAS*, 270, 121
 Hillwig T. C., Jones D., De Marco O., Bond H. E., Margheim S., Frew D., 2016, *ApJ*, 832, 125
 Iaconi R., Reichardt T., Staff J., De Marco O., Passy J.-C., Price D., Wurster J., Herwig F., 2017, *MNRAS*, 464, 4028
 Iaconi R., De Marco O., Passy J.-C., Staff J., 2018, *MNRAS*, 477, 2349
 Ivanova N., 2018, *ApJ*, 858, L24
 Kuruwita R. L., Staff J., De Marco O., 2016, *MNRAS*, 461, 486
 MacLeod M., Macias P., Ramirez-Ruiz E., Grindlay J., Batta A., Montes G., 2017a, *ApJ*, 835, 282
 MacLeod M., Antoni A., Murguia-Berthier A., Macias P., Ramirez-Ruiz E., 2017b, *ApJ*, 838, 56
 MacLeod M., Ostriker E. C., Stone J. M., 2018a, *ApJ*, 868, 136
 MacLeod M., Ostriker E. C., Stone J. M., 2018b, *ApJ*, 863, 5
 Meakin C. A., Biegging J. H., Latter W. B., Hora J. L., Tielens A. G. G. M., 2003, *ApJ*, 585, 482
 Metzger B. D., Pejcha O., 2017, *MNRAS*, 471, 3200
 Miszalski B., Acker A., Moffat A. F. J., Parker Q. A., Udalski A., 2009, *A&A*, 496, 813
 Nandez J. L. A., Ivanova N., 2016, *MNRAS*, 460, 3992
 Nandez J. L. A., Ivanova N., Lombardi J. C., Jr., 2014, *ApJ*, 786, 39
 Nandez J. L. A., Ivanova N., Lombardi J. C., 2015, *MNRAS*, 450, L39
 Ohlmann S. T., Röpke F. K., Pakmor R., Springel V., 2016, *ApJ*, 816, L9
 Paczynski B., 1976, in Eggleton P., Mitton S., Whelan J., eds, *IAU Symp. Vol. 73, Structure and Evolution of Close Binary Systems*. Kluwer, Dordrecht, p. 75
 Paczyński B., Sienkiewicz R., 1972, *Acta Astron.*, 22, 73
 Passy J.-C. et al., 2012, *ApJ*, 744, 52
 Pejcha O., Metzger B. D., Tomida K., 2016, *MNRAS*, 461, 2527
 Pejcha O., Metzger B. D., Tyles J. G., Tomida K., 2017, *ApJ*, 850, 59
 Price D. J. et al., 2018, *PASA*, 35, e031
 Price D. J., 2007, *PASA*, 24, 159
 Ricker P. M., Taam R. E., 2012, *ApJ*, 746, 74
 Ritter H., 1988, *A&A*, 202, 93
 Shima E., Matsuda T., Takeda H., Sawada K., 1985, *MNRAS*, 217, 367
 Smith N. et al., 2016, *MNRAS*, 458, 950
 Soker N., 2017, *MNRAS*, 471, 4839
 Soker N., Grichener A., Sabach E., 2018, *ApJ*, 863, L14
 Staff J. E., De Marco O., Macdonald D., Galaviz P., Passy J.-C., Iaconi R., Low M.-M. M., 2016a, *MNRAS*, 455, 3511
 Staff J. E., De Marco O., Wood P., Galaviz P., Passy J.-C., 2016b, *MNRAS*, 458, 832
 Tocknell J., De Marco O., Wardle M., 2014, *MNRAS*, 439, 2014
 Toonen S., Nelemans G., 2013, *A&A*, 557, A87
 Tout C. A., Hall D. S., 1991, *MNRAS*, 253, 9
 Tylenda R. et al., 2011, *A&A*, 528, A114
 van Winckel H. et al., 2009, *A&A*, 505, 1221

This paper has been typeset from a $\text{\TeX}/\text{\LaTeX}$ file prepared by the author.